HHS Public Access

Author manuscript

J Biomed Nanotechnol. Author manuscript; available in PMC 2022 April 26.

Published in final edited form as:

J Biomed Nanotechnol. 2015 August ; 11(8): 1442–1450. doi:10.1166/jbn.2015.2089.

Photoacoustic- and Magnetic Resonance-Guided Photothermal Therapy and Tumor Vasculature Visualization Using Theranostic Magnetic Gold Nanoshells

Min Zhou[1], **Burapol Singhana**[2], **Yang Liu**[2], **Qian Huang**[1], **Trevor Mitcham**[3], **Michael J. Wallace**[2], **R. Jason Stafford**[3,4], **Richard R. Bouchard**[3,4], **Marites P. Melancon**[2,3,*]

[1]Department of Cancer Systems Imaging, The University of Texas MD Anderson Cancer Center, Houston, Texas 77030, USA

[2]Department of Interventional Radiology, The University of Texas MD Anderson Cancer Center, Houston, Texas 77030, USA

[3]Department of Imaging Physics, The University of Texas MD Anderson Cancer Center, Houston, Texas 77030, USA

[4]The University of Texas Graduate School of Biomedical Science, Houston, TX 77030, USA

Abstract

Nanoparticle based image-guided therapy is an emerging technology for cancer in recent years. Here, we report simultaneous photoacoustic (PA)- and magnetic resonance (MR)-guided photothermal ablation (PTA) therapy using multifunctional superparamagnetic iron oxide-containing gold nanoshells (SPIO@AuNS). Based on the intrinsic high near-infrared optical absorbance and strong magnetic property of SPIO@AuNS, we carried out *in vivo* dual-modality PA-MR imaging of mouse tumors. PA- and MR-guided imaging can monitor therapeutic effect after photothermal therapy mediated by our multifunctional nanomaterial. In addition, using our pulsed laser PA technique, we also observe a clearer structure of the tumor vasculature after intravenously administration SPIO@AuNS. The novel dual PA-MRI image-guided PTA therapy provides a promising new platform for cancer diagnosis and treatment simultaneously.

Keywords

Nanoparticles; Photoacoustic Imaging; Magnetic Resonance Imaging; Photothermal Therapy; Imaging Guided Therapy

INTRODUCTION

Image-guided thermal ablation of tumors is becoming a more widely accepted minimally invasive alternative to surgery for patients who are not good surgical candidates.[1–3] Laser ablation has been shown to be mediated efficiently by plasmonic gold nanomaterials,[4–6] carbon nanotubes,[7, 8] copper sulfide nanomaterials,[9] or other nanoparticulate materials,[10–12]

*Author to whom correspondence should be addressed. mmelancon@mdanderson.org.

all of which can be made to preferentially home to tumor tissue and strongly absorb near-infrared (NIR) light. Absorption in the NIR region is highly desirable because water and naturally occurring fluorochromes have the lowest absorption in this region, and therefore light can penetrate deeper into the tissues. Clinical trials are currently being conducted to investigate the use of silica-containing gold nanospheres in NIR photothermal ablation (PTA) therapy for refractory head-and-neck and lung cancers.[13] However, to ensure the safety and efficacy of this type of thermal ablation therapy, one must (i) confirm that the nanoparticles have been delivered to the target tissue, and (ii) determine the amount of nanoparticles accumulated in the target tissue as a way to correlate nanoparticle concentration with corresponding tissue damage for pretreatment planning and for noninvasive real-time monitoring of the spatiotemporal heat profile and of response to therapy in a given target volume.

Magnetic resonance imaging (MRI) has become a prominent noninvasive technique in diagnostic clinical medicine because it can provide highly resolved three-dimensional images of living bodies.[14, 15] Recently, we explored MR-guided nanoparticle-mediated PTA cancer therapy. MRI is sensitive to nanoscale contrast agents and can provide real-time temperature-sensitive feedback during therapy.[16, 17]

Photoacoustic (PA) imaging, also referred to as optoacoustic imaging, is based on the measurement of ultrasonic waves induced by biological tissues' or inorganic materials absorption of short laser pulses.[18] Photoacoustic imaging employs nonionizing laser light to acoustically visualize biological tissues with high optical contrast and high ultrasonic resolution. When tissue samples are heated, ultrasound echoes shift because of the change in the speed of sound and thermal expansion of the tissue. Currently, preclinical systems for PA imaging can provide images *in vivo* and in real time using a tunable light source at 680–970 nm in combination with an ultrasound system. As a relatively new non-invasive approach, PA tumor imaging systems has been widely researched and has promising clinical applications.[18]

Magnetic plasmonic nanomaterials have shown great potential in the development of MRI-guided anticancer PTA therapy because of these materials' unique optical and magnetic properties.[17, 19] Among them, SPIO-containing gold nanoshells (SPIO@AuNS) are particularly interesting because of their strong magnetic property and tunable resonance in the NIR spectrum, where the optical window permits photon penetration into biological tissues with relatively high transitivity.[20]

MRI, as a well-established imaging method, has some limitations for clinic use due to its low sensitivity and specificity,[21] and the new emerging non-invasive PA technique also need for improvement for the depth and resolution limits.[22] The combination of MR and PA bimodal imaging would be at advantage to obtaine simultaneous structural and functional information with high resolution and sensitivity. Moreover, bimodal MR-PA agents are also conceived potentially for diagnostic imaging and therapy of cancer application. Because the generation of acoustic signal is due to the thermoelastic expansion of the PA contrast agents, it is possible to elevate the temperature of the target tumor tissue by increasing the intensity of the incident laser beam, causing significant damage to tumor tissue.[23] As a

proof-of-concept, we investigated in this study, a new application, such as PA imaging, of the SPIO@AuNS for their multifunctional theranostic cancer applications. Using PA and MRI, we investigated SPIO@AuNS as a contrast agent for anticancer imaging guided PTA therapy in live mice and for imaging tumor blood vasculature. Our findings indicate that SPIO@AuNS can be used to improve the efficacy of cancer diagnosis and therapy.

EXPERIMENTAL SECTION

Chemicals

Methoxy-polyethylene glycol-sulfhydryl (molecular weight 5000 Da) and phosphate-buffered saline (PBS pH 7.4) were purchased from Sigma-Aldrich (St. Louis, MO). PD-10 columns were purchased from GE Healthcare (Piscataway, NJ). Trisodium citrate dihydrate (>99%) and chloroauric acid trihydrate (American Chemical Society reagent grade) were purchased from Fisher Scientific (Pittsburgh, PA) and used without further purification. SPIO (EMG 304) was purchased from FerroTec (Bedford, NH).

Synthesis and Characterization of SPIO@AuNS

SPIO@AuNS were prepared as described elsewhere.[20] Briefly, 10-nm-diameter SPIO nanoparticles were first coated with a layer of amorphous silica via the sol–gel method. Next, gold nanocrystals 2 to 3 nm in diameter were deposited on the amine-modified silica surface of the nanoparticles. The gold nanocrystals served as the seeds mediating nucleation and growth of a gold overlayer to produce the SPIO@AuNS. The particles were subjected to centrifugation at 8,000 rpm for 15 min, washed with deionized water three times, and re-suspended in water. Polyethylene glycol with thiol group (MW = 5000) was then added to the SPIO@AuNS and reacted overnight at 4 °C, washed with water the next day, and resuspended in PBS. The SPIO@AuNS were characterized in terms of size, morphology, composition, optical absorption, and magnetization. For the transmission electron microscopy study, SPIO@AuNS were applied to a 100-mesh nickel grid coated with a polyvinyl formvar resin and carbon (Ted Pella, Redding, CA). The nanoparticles were allowed to attach to the grid for 1 h, after which the grid was rinsed with deionized water and dried in air. The samples were examined using a transmission electron microscope (JEM 2100F, JEOL Ltd., Akishima, Japan) at an accelerating voltage of 200 kV. The average size and thickness of the gold layer were calculated for at least 50 particles. The elemental composition of SPIO@AuNS was determined by using an energy-dispersive X-ray spectrometer attached to the JEM 2100F transmission electron microscope. Size in solution was determined using ZetaPlus Zeta Potential Analyzer (Brookhaven Instruments Corporation, Holsville, NY). UV-visible light spectroscopy was recorded on a Beckman Coulter DU800 UV-Vis spectrophotometer using a 1-cm optical path length quartz cuvette. The Vevo LAZR-2100 PAUS imaging system (VisualSonics Inc., Ontario, Canada) was used to measure the PA signal at different wavelengths (650–950 nm). Lastly, the concentrations of iron and gold in the SPIO@AuNS suspension were measured using an inductively coupled plasma mass spectrometer (Galbraith Laboratories, Inc., Knoxville, TN).

In Vitro MRI

MR images of SPIO@AuNS samples at different concentrations were obtained with a 1.5 T clinical MRI scanner (Excite HD GE Healthcare, Waukesha, WI) and the BioSpec 4.7 T experimental MRI system (Bruker BioSpin MRI, Billerica, MA). Parameters were as follows: fast spin echo sequence with 24 echo time (TE) values ranging from 15 to 360 ms, repetition time (TR) = 1000 ms, field of view = 3.2 cm, slice thickness = 1 mm, acquisition matrix = 64 × 64. T_2 values were calculated as the slope from a linear least-square line fit to the log of the mean measured MR signal in a region of interest versus TE.

Phantom Photoacoustic Imaging

Photoacoustic spectroscopy was performed with the Vevo LAZR-2100 PAUS imaging system. A 24-mm-wide, 21-MHz linear acoustic array transducer was used for signal detection and was coupled to the LAZR-2100 system for sample irradiation. Changes in the PA signal were measured by scanning at 680–970 nm.

Photoacoustic Imaging of Different Nanomaterials

To compare the effective PA signals of different nanomaterials, agarose gels containing SPIO@AuNS, gold nanorods (Aspect ratio ~3, Nanopartz, Loveland, CO), or carbon nanotubes (Nanoamor, Houston, TX) or containing gel only was embedded in a section of chicken breast muscle, which was then placed under other pieces of chicken breast muscle, each approximately 1.0 cm thick. An inhouse PA tomography system comprising a Q-switched Nd:YAG laser (LS-2137/2 LOTIS TII) and a pumped tunable Ti:sapphire laser (LT-2211A LOTIS TII) was employed to excite PA signals for the different nanoparticles. The lasers had a pulse duration of <15 ns, a pulse repetition rate of 10 Hz, and a wavelength of 800 nm. The incident energy density of the laser beam was kept at <10 mJ/cm^2 on the surface of the chicken breast. An unfocused ultrasonic transducer (V323, Panametrics) with a central frequency of 2.25 MHz and a −6-dB bandwidth of about 70% was used to detect the ultrasound signals (acquisition time 10 min). The PA signals detected by the ultrasonic transducer were amplified (5072PR pulser-receiver Olympus). The PA images were reconstructed by a modified back-projection algorithm.

In Vivo Imaging and Photothermal Therapy

All animal studies were carried out in the Small Animal Imaging Facility at The University of Texas MD Anderson Cancer Center under Institutional Animal Care and Use Committee-approved protocols. Female nude mice were purchased from Experimental Radiation Oncology breeding at The University of Texas MD Anderson Cancer Center (Houston, TX). To create the mouse tumor model, we injected breast 4T1 cells (5 × 10^5, 100 μl) subcutaneously into each flank of female mice. Experiments were conducted after the tumors grew to 0.6–0.8 cm in diameter. Two separate experiments were done. One experiment used the Vevo LAZR-2100 PAUS imaging system for detecting increases in the PA signal with B-mode ultrasound imaging, and the second experiment used MRI and MR temperature imaging (MRTI). In both experiments, changes in signal (PA or T_2^* MRI) and temperature were determined.

The Vevo LAZR system is coupled with a 21-MHz, 24 mm-wide linear acoustic array transducer to allow simultaneous imaging of the PA signal with B-mode ultrasound. Three mice were each injected intratumorally with SPIO@AuNS (aqueous solution, 25 μl, 1.32 × 10^{11} particles/ml, 6.7 μg (Fe)/mL.). Using an integrated ultrasonogram, a B-mode image was acquired, and then the PA signal was recorded before (40 s), during (90 s), and after (60 s) laser treatment. An 808-nm NIR laser (Diomed 15 Plus, Biolitec, Cambridge, UK) (5-mm spot diameter) was used to irradiate the tumor at an output power of 3 W (0.15 W/mm^2) for 90 s. To correlate the increase in PA signal amplitude with temperature, a separate experiment was done using phantoms containing SPIO@AuNS. The PA phantom was constructed as previously described.[24] In brief, a plastic tube was filled with SPIO@AuNS (optical density 5), tube ends were sealed with epoxy, and the tube was suspended in a water-filled plastic tub. The water bath containing the phantom was heated from 21 °C to 70 °C, and the phantom was imaged at a laser wavelength of 808 nm. The PA signal was monitored using the PA system, and a Fluoroptic temperature probe coupled to an m3300 Fluoroptic thermometer (LumaSense Technologies Inc., Santa Clara, CA) was used to monitor temperature. The increase in the PA signal with respect to time was plotted, and the equation of the line was used to convert the PA signal to temperature.

In a separate experiment, five mice were imaged using a 1.5 T MRI scanner (Excite HD) after intratumoral injection of SPIO@AuNS (1.32 × 10^{11} particles/ml, 25 μl). Saline was used as a control. A multiple, fast-gradient, refocused echo was used, with 16 echoes ranging from 2 to 60 ms for each TR. T_2^* maps were calculated using the Steiglitz-McBride algorithm, which was recently shown to provide accurate and precise T_2^* estimates, even in the presence of lipids. This technique also calculates the proton resonance frequency to estimate temperature changes, thereby providing simultaneous T_2^* mapping and MRTI. Mice were imaged before (30 s), during (3 min), and after NIR laser irradiation (4 W/cm^2, 808 nm) using the Diomed 15 Plus laser.

Histology

At the end of each imaging experiment, mice were killed by cervical dislocation, and tumors were collected and fixed in formalin. Tumors were cut into 5-μm sections and stained with hematoxylin and eosin. Two to four slices of each tumor were analyzed to determine the percentage of tumor necrosis. Image J software was used to calculate the percentage of tumor necrosis, which was defined as area of necrosis/area of entire tumor × 100.

Vascular Imaging Using Pulsed Laser PA Tomography

For vascular imaging, three mice bearing 4T1 tumors were each injected intravenously with SPIO@AuNS (1.32 × 10^{11} particles/ml, 25 μl). PA imaging was done before and 2 h after nanoparticle injection. For PA imaging of tumor vasculature, the Q-switched Nd:YAG laser (LS-2137/2) and pumped tunable Ti:sapphire laser (LT-2211A) were employed. The incident energy density of the laser beam was kept at <10 mJ/cm^2 on the surface of the mouse tumor. Experimental set-up is illustrated in Supporting Information, Figure S1.

Statistical Analysis

Results were analyzed using a two-tailed unpaired Student *t* test or one-way analysis of variance $p < 0.05$ considered statistically significant.

RESULTS AND DISCUSSION

Synthesis and Characterization of SPIO@AuNS

Plasmonic core–shell magnetic nanomaterials composed of SPIO coated with a gold layer can both reduce the toxicity of the iron oxide core and offer potential opportunity for multifunctional theranostic applications. Figure 1(A) illustrates the structure of SPIO@AuNS. The particles have an SPIO core in a layer of silica that is coated with gold on the surface. The representative transmission electron micrograph in Figure 1(B) shows an average-size SPIO@AuNS particle of ~90 nm in diameter as determined by TEM. Energy-dispersive X-ray spectroscopy confirmed the presence of gold, iron, and silica (Fig. 1(C)) in the synthesized SPIO@AuNS. Figure 1(D) shows the size distribution of SPIO@AuNS in solution using the dynamic light scattering (DLS). Using the DLS, the average diameter was measured to be 85.2 nm with polydiversity index (PDI) of 0.159. The optical absorption spectrum of SPIO@AuNS is shown in Figure 1(E). The peak of absorption is at 700–900 nm, and when the phtoacoustic signal is acquired at different wavelengths (Fig. 1(F)), the peak intensity corresponds to the UV-visible absorption spectrum. These characteristics confirm the suitability of SPIO@AuNS for PA imaging in the NIR region. Moreover, SPIO@AuNS exhibited excellent colloidal stability, as no apparent aggregation was observed when the nanoshells were stored in PBS buffer at 4 °C for 2 weeks. DLS also confirmed that no size change was observed even after 2 weeks of storage. The SPIO@AuNS concentration was calculated from the volume of each NS and from the gold concentration, which was determined by inductively coupled plasma mass spectrometry.

Magnetic Properties of SPIO@AuNS

The potential of SPIO@AuNS as an MRI contrast agent was first examined using a 4.7 T MRI scanner. Figure 2(A) shows the MR signal-enhancing capability of SPIO@AuNS in water as a function of iron concentration. With increased iron concentration, the measured T_2-weighted image contrast gradually darkens. Figure 2(B) shows the corresponding transverse relaxation ($1/T_2$) of protons in the particle solution as a function of iron concentration, obtained with the 1.5 T clinical MRI scanner. Figure 2(C) shows the calculated R_2 values of SPIO@AuNS compared with the R_2 values of the Food Drug Administration-approved MRI contrast agent ferumoxide (Feridex™) at 1.5 T (208 vs. 171 $mM^{-1}\ s^{-1}$) and 4.7 T (369 vs. 240 $mM^{-1}\ s^{-1}$). The R_2 values of SPIO@AuNS at both 1.5 T and 4.7 T were comparable to and slightly higher than those of Feridex under the same magnetic field intensity. The slightly higher values for SPIO@AuNS are consistent with the previous finding that larger particles yield darker images with T_2 weighting.[20]

Photoacoustic Signal of SPIO@AuNS

Photoacoustic imaging is based on the PA effect of light-absorbers and offers remarkably greater image depth than does traditional optical imaging. Several nanomaterials have also been proposed as contrast agents for PA imaging, including gold nanorods (AuRods)[25–27] and single-wall carbon nanotubes (SWNTs).[23, 28, 29] We compared the performance of SPIO@AuNS, AuRods, and SWNTs by using PA signals acquired at a wavelength of 808 nm. Three agarose gels containing 100 μg/mL of SPIO@AuNS, AuRods, or SWNTs and a control gel without any contrast agent were embedded counterclockwise starting at the 1 o'clock position in a 1-cm-thick piece of chicken breast muscle (Fig. 3(A)). Figure 3(B) shows the absorption spectrum of the three agents used in Figure 3(A). Figure 3(C) PA images obtained at a depth of 1 cm. The agarose gel containing 100 μg/mL of SPIO@AuNS was clearly visualized. The agarose gels containing 100 μg/mL of AuRods or SWNTs were also visualized, albeit at much lower signal intensity. The PA signal of SPIO@AuNS was approximately 4 and 3 times greater than the PA signals of AuRods and SWNTs, respectively. No signal could be detected for the control gel. These data indicate that SPIO@AuNS are well suited as a contrast agent for *in vivo* PA.

In Vivo PA and MRI

We next used SPIO@AuNS as a multimodal imaging probe for *in vivo* imaging of mouse tumors. As a proof-of-concept experiment, we evaluated the *in vivo* contrast-enhancing effect of SPIO@AuNS for MR and PA imaging in mice. Female nude mice bearing 4T1 tumors were intratumorally injected with SPIO@AuNS and imaged by PA and MRI systems in two separate experiments.

In the first experiment, mice (n = 3) were intratumorally injected with SPIO@AuNS (50 μL, optical density 5) and imaged by a Vevo LAZR PA imaging system with an 808-nm laser as the excitation source. Ultrasound and PA dual-modality images of a cross section across the center of the tumor were obtained before the injection, and changes were monitored thereafter. The ultrasound image was used to visualize the boundaries of the tumor, such as the skin and tumor tissue, as well as to confirm the site of the tumor (Fig. 4(A)). The PA image was used to gauge the contrast achieved with the nanomaterial in the tumor tissue (Fig. 4(B)). The two imaging modalities used the same instrumentation and provided complementary information. After the SPIO@AuNS injection, the PA signal in the tumor was clearly visible (Fig. 4(C)). The relative weakness of the signal in portions of the tumor is presumably due to the optical absorption by the tumor's blood content at 808 nm. The prominent signals indicated by the arrow in Figure 4(D) indicate high concentrations of SPIO@AuNS in those areas. During the laser irradiation, we observed a 25% increase in signal amplitude, corresponding to a temperature of about 55 °C (Figs. 4(E), (F)), which is sufficient to ablate tumors.

In a separate experiment, we assessed the MR-mediating capability of SPIO@AuNS. Figure 5 shows the darkening effect of the nanoparticles in the tumors. Figures 5(A) and (B) show the T_2^* map of a tumor before and after intratumoral injection of SPIO@AuNS, respectively. In agreement with the PA imaging results, significant darkening of the tumor was visible in the presence of SPIO@AuNS. T_2^* values decreased from 21.1 ± 2.8 ms preinjection to 9.4

± 1.0 ms postinjection. T_2^* values remained unchanged (9.3 ± 1.2 ms) after laser irradiation (Fig. 5(C)).

Figure 5(D) shows a representative MRTI map of the tumor immediately after laser irradiation. Figure 5(E) shows the temperatures observed with or without SPIO@AuNS before, during, and after laser irradiation. Tumors injected with SPIO@AuNS had a greater increase in temperature than did tumors injected with saline. The temperature increased to about 65 °C in SPIO@AuNS-injected tumors and only to 42 °C in saline-injected tumors. Also, the temperature increased more on the outer surfaces of the tumors than inside the tumors.

Of the different imaging modalities, MRI appears to be the ideal tool for temperature mapping. A particular advantage of MRI for guiding thermal procedures is that MRI not only allows temperature mapping but also can be used for target definition, and it may aid early evaluation of therapeutic efficacy. Several MR parameters—relaxation times (T_1 and T_2), bulk magnetization, and proton resonance frequency—are temperature sensitive. The latter has been shown to be especially sensitive to temperature and is most commonly used to monitor temperature change during thermal ablation, with temperature errors limited to 0.5–1 °C.

Histological Analysis

In our PA and MRI studies, the observed temperature variations were sufficient to induce irreversible tissue damage. The therapeutic effects of SPIO@AuNS-mediated photothermal therapy were further demonstrated by histopathological analysis (Fig. 6). After irradiation, control specimens showed no difference in cell size or shape, no nuclear modifications, and no necrosis. This finding indicates that the PBS heating induced by the 808-nm laser irradiation, corresponding to a temperature rise of only 2 °C, was not enough to kill the cancer cells. In contrast, SPIO@AuNS-treated cells showed thermal cell necrosis, as evidenced by reduced size, loss of contact, eosinophilic cytoplasm, and nuclear damage. The difference between the necrosis percentage in SPIO@AuNS-injected tumors irradiated with a surface laser probe and the necrosis percentage in SPIO@AuNS-injected tumors that were not irradiated was statistically significant (91% vs. 3.2% $p < 0.0001$). These findings indicate that SPIO@AuNS have excellent potential as a therapeutic agent for PTA of tumor tissues.

PA Tomographic Imaging of Tumor Blood Vasculature

Because antiangiogenic cancer therapies are designed to affect abnormal blood vessels within tumors, morphological changes in tumor vasculature and changes in hemo-dynamic parameters such as blood flow, blood volume, or vessel permeability may be promising biomarkers for evaluating therapeutic effects. Therefore, *in vivo* study of tumor blood vasculature is of vital importance to fundamental cancer research and to the development of new drugs and therapies. Although the commercial Vevo LAZR-2100 PAUS imaging system can visualize the tumor and surrounding tissues, its relatively low sensitivity limits its clinical applicability. Our custom-made PA imaging system, which uses a pulse laser, can improve the sensitivity.[30] Figure 7(A) shows a representative *in vivo* PA image of

the blood vessel structure of a mouse 4T1 breast tumor acquired at 808 nm without a contrast agent. Several large vessels can be seen because of the light absorption of the hemoglobin. However, smaller blood vessels are not discernible. Two hours after intravenous administration of SPIO@AuNS, blood vessel structures, including smaller vessels, were more clearly visible (Fig. 7(B)). These results indicate that SPIO@AuNS are a promising contrast agent for PA imaging of tumor blood vessels.

CONCLUSION

PA- and MR-guided SPIO@AuNS PTA therapy were investigated owing to their high NIR optical absorbance and strong magnetic properties. In our proof-of-concept study, the photothermal ablation therapeutic effects of tumor in mice were monitored by PA- and MR dual imaging technologies. Moreover, SPIO@AuNS can significantly enhanced the visualization of tumor blood vasculature using our pulsed laser PA technique. Future studies will focus on multimodality imaging guided photothermal therapy after intravenous administration of SPIO@AuNS. We conclude that SPIO@AuNS have excellent potential for use in PA- and MR-guided PTA therapy and in the development of advanced anticancer theranostics.

Acknowledgments:

This work was supported in part by grants from the Odyssey Fellowship (to M. P. M and R. R. B), John S. Dunn Foundation, and National Institutes of Health (1S10OD010403-1) and by MD Anderson's Cancer Center Support Grant CA016672 for the small-animal imaging and veterinary pathology core facilities.

REFERENCES

1. Boppart SA, Herrmann J, Pitris C, Stamper DL, Brezinski ME, and Fujimoto JG, High-resolution optical coherence tomography-guided laser ablation of surgical tissue. J. Surg. Res, 82, 275 (1999). [PubMed: 10090840]
2. Gronemeyer DHW, Schirp S, and Gevargez A, Image-guided radiofrequency ablation of spinal tumors: Preliminary experience with an expandable array electrode. Cancer J. 8, 33 (2002). [PubMed: 11898806]
3. Lindner U, Weersink RA, Haider MA, Gertner MR, Davidson SRH, Atri M, Wilson BC, Fenster A, and Trachtenberg J, Image guided photothermal focal therapy for localized prostate cancer: Phase I trial. J. Urology 182, 1371 (2009).
4. Hirsch LR, Stafford RJ, Bankson JA, Sershen SR, Rivera B, Price RE, Hazle JD, Halas NJ, and West JL, Nanoshell-mediated near-infrared thermal therapy of tumors under magnetic resonance guidance. P. Natl. Acad. Sci. USA 100, 13549 (2003).
5. Huang XH, El-Sayed IH, Qian W, and El-Sayed MA, Cancer cell imaging and photothermal therapy in the near-infrared region by using gold nanorods. J. Am. Chem. Soc 128, 2115 (2006). [PubMed: 16464114]
6. Melancon MP, Lu W, Yang Z, Zhang R, Cheng Z, Elliot AM, Stafford J, Olson T, Zhang JZ, and Li C, *In vitro* and *in vivo* targeting of hollow gold nanoshells directed at epidermal growth factor receptor for photothermal ablation therapy. Mol. Cancer Ther 7, 1730 (2008). [PubMed: 18566244]
7. Chakravarty P, Marches R, Zimmerman NS, Swafford ADE, Bajaj P, Musselman IH, Pantano P, Draper RK, and Vitetta ES, Thermal ablation of tumor cells with anti body-functionalized single-walled carbon nanotubes. P. Natl. Acad. Sci. USA 105, 8697 (2008).
8. Moon HK, Lee SH, and Choi HC, *In vivo* near-infrared mediated tumor destruction by photothermal effect of carbon nanotubes. Acs Nano 3, 3707 (2009). [PubMed: 19877694]

9. Zhou M, Zhang R, Huang MA, Lu W, Song SL, Melancon MP, Tian M, Liang D, and Li C, A chelator-free multifunctional [Cu-64]CuS nanoparticle platform for simultaneous micro-PET/CT imaging and photothermal ablation therapy. J. Am. Chem. Soc 132, 15351 (2010). [PubMed: 20942456]
10. Cheng L, Yang K, Chen Q, and Liu Z, Organic stealth nanoparticles for highly effective *in vivo* near-infrared photothermal therapy of cancer. Acs Nano 6, 5605 (2012). [PubMed: 22616847]
11. Chen ZG, Wang Q, Wang HL, Zhang LS, Song GS, Song LL, Hu JQ, Wang HZ, Liu JS, Zhu MF, and Zhao D, Ultrathin PEGylated $W_{18}O_{49}$ nanowires as a new 980 nm-laser-driven photothermal agent for efficient ablation of cancer cells *in vivo*. Adv. Mater 25, 2095 (2013). [PubMed: 23427112]
12. Liu YL, Ai KL, Liu JH, Deng M, He YY, and Lu LH, Dopamine-melanin colloidal nanospheres: An efficient near-infrared photothermal therapeutic agent for *in vivo* cancer therapy. Adv. Mater 25, 1353 (2013). [PubMed: 23280690]
13. El-Sayed IH, Nanotechnology in head and neck cancer: The race is on. Curr. Oncol. Rep 12, 121 (2010). [PubMed: 20425597]
14. Na HB, Song IC, and Hyeon T, Inorganic nanoparticles for MRI contrast agents. Adv. Mater 21, 2133 (2009).
15. Sereno MI, Dale AM, Reppas JB, Kwong KK, Belliveau JW, Brady TJ, Rosen BR, and Tootell RBH, Borders of multiple visual areas in humans revealed by functional magnetic-resonance-imaging. Science 268, 889 (1995). [PubMed: 7754376]
16. Melancon MP, Elliott A, Ji XJ, Shetty A, Yang Z, Tian M, Taylor B, Stafford RJ, and Li C, Theranostics with multifunctional magnetic gold nanoshells photothermal therapy and T_2^* magnetic resonance imaging. Invest. Radiol 46, 132 (2011). [PubMed: 21150791]
17. Melancon MP, Lu W, Zhong M, Zhou M, Liang G, Elliott AM, Hazle JD, Myers JN, Li C, and Stafford RJ, Targeted multifunctional gold-based nanoshells for magnetic resonance-guided laser ablation of head and neck cancer. Biomaterials 32, 7600 (2011). [PubMed: 21745689]
18. Wang XD, Pang YJ, Ku G, Xie XY, Stoica G, and Wang LHV, Noninvasive laser-induced photoacoustic tomography for structural and functional *in vivo* imaging of the brain. Nat. Biotechnol 21, 803 (2003). [PubMed: 12808463]
19. Tian QW, Hu TQ, Zhu YH, Zou RJ, Chen ZG, Yang SP, Li RW, Su QQ, Han Y, and Liu XG, Sub-10 nm Fe_3O_4@Cu_2-xS core–shell nanoparticles for dual-modal imaging and photothermal therapy. J. Am. Chem. Soc 135, 8571 (2013). [PubMed: 23687972]
20. Ji XJ, Shao RP, Elliott AM, Stafford RJ, Esparza-Coss E, Bankson JA, Liang G, Luo ZP, Park K, Markert JT, and Li C, Bifunctional gold nanoshells with a superparamagnetic iron oxide-silica core suitable for both MR imaging and photothermal therapy. J. Phys. Chem. C 111, 6245 (2007).
21. Geninatti-Crich S, Lanzardo S, Alberti D, and Aime S, MR "*in vivo*" preclinical molecular and cellular imaging. Minerva Biotecnol 21, 111 (2009).
22. Wang LV, Prospects of photoacoustic tomography. Med. Phys 35, 5758 (2008). [PubMed: 19175133]
23. Kang B, Yu DC, Dai YD, Chang SQ, Chen D, and Ding YT, Cancer-cell targeting and photoacoustic therapy using carbon nanotubes as "bomb" agents. Small 5, 1292 (2009). [PubMed: 19274646]
24. Lee HJ, Liu Y, Zhao J, Zhou M, Bouchard RR, Mitcham T, Wallace MJ, Stafford RJ, Li C, Gupta S, and Melancon MP, *In vitro* and *in vivo* mapping of drug release after laser ablation thermal therapy with doxorubicin-loaded hollow gold nanoshells using fluorescence and photoacoustic imaging. J. Control Release 172, 152 (2013). [PubMed: 23920038]
25. Li PC, Huang SW, Wei CW, Chiou YC, Chen CD, and Wang CRC, Photoacoustic flow measurements by use of laser-induced shape transitions of gold nanorods. Opt. Lett 30, 3341 (2005). [PubMed: 16389825]
26. Chen YS, Frey W, Kim S, Kruizinga P, Homan K, and Emelianov S, Silica-coated gold nanorods as photoacoustic signal nanoamplifiers. Nano Lett. 11, 348 (2011). [PubMed: 21244082]
27. Jokerst JV, Cole AJ, Van de Sompel D, and Gambhir SS, Gold nanorods for ovarian cancer detection with photoacoustic imaging and resection guidance via raman imaging in living mice. Acs Nano 6, 10366 (2012). [PubMed: 23101432]

28. Wang C, Ma XX, Ye SQ, Cheng L, Yang K, Guo L, Li CH, Li YG, and Liu Z, Protamine functionalized single-walled carbon nanotubes for stem cell labeling and *in vivo* raman/magnetic resonance/photoacoustic triple-modal imaging. Adv. Funct. Mater 22, 2363 (2012).

29. De La Zerda A, Zavaleta C, Keren S, Vaithilingam S, Bodapati S, Liu Z, Levi J, Smith BR, Ma TJ, Oralkan O, Cheng Z, Chen X, Dai H, Khuri-Yakub B, and Gambhir SS, Carbon nanotubes as photoacoustic molecular imaging agents in living mice. Nat. Nanotechnol 3, 557 (2008). [PubMed: 18772918]

30. Ku G, Zhou M, Song SL, Huang Q, Hazle J, and Li C, Copper sulfide nanoparticles as a new class of photoacoustic contrast agent for deep tissue imaging at 1064 nm. Acs Nano 6, 7489 (2012). [PubMed: 22812694]

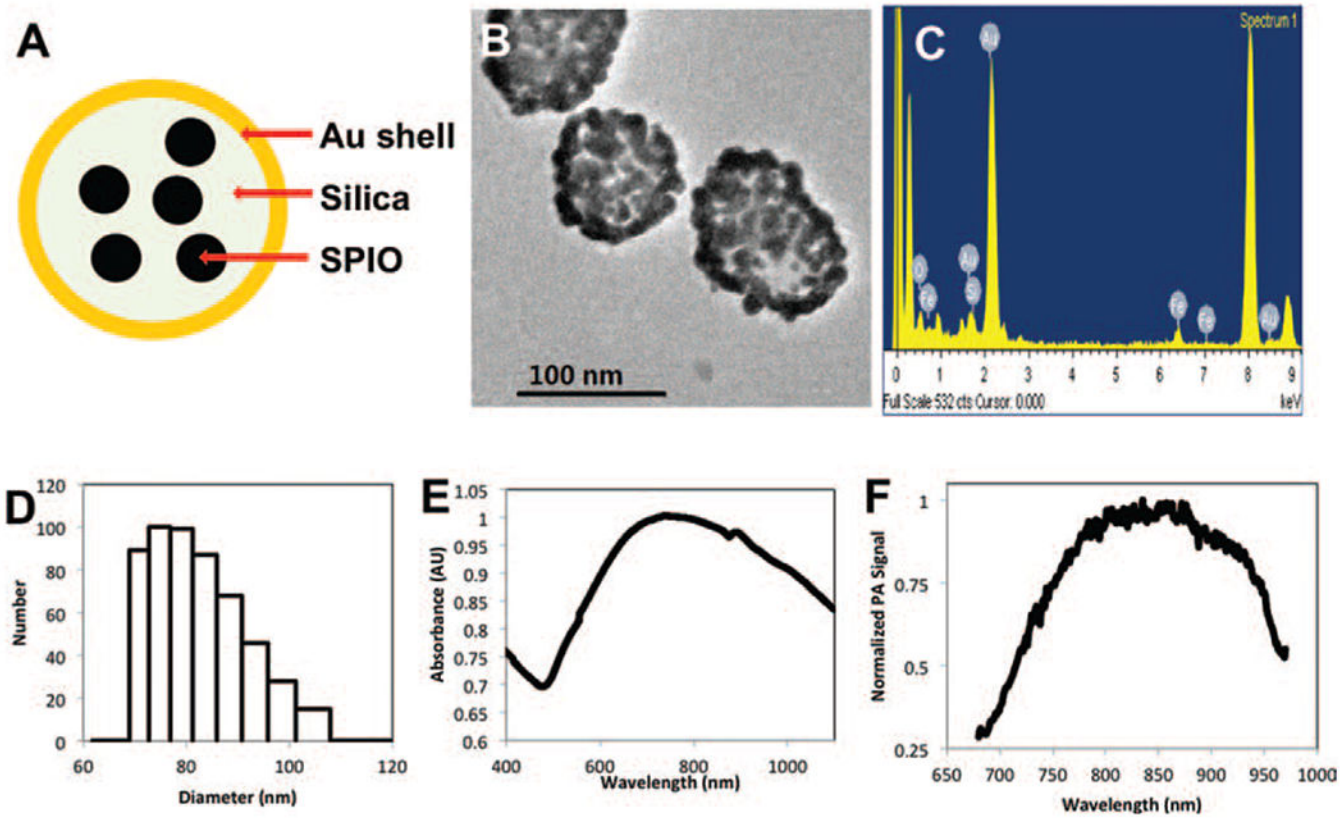

Figure 1.

SPIO@AuNS structure (A), transmission electron micrograph [TEM] image (B), energy dispersive X-ray spectrum (C), dynamic light scattering [DLS] size distribution (D), UV-visible spectrum (E), and photoacoustic (PA) spectrum (F). AU: absorbance units.

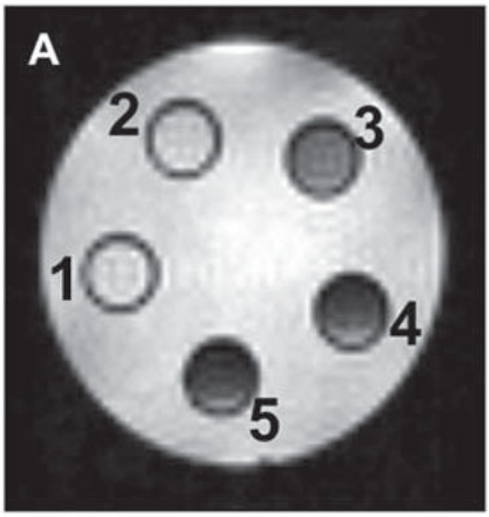

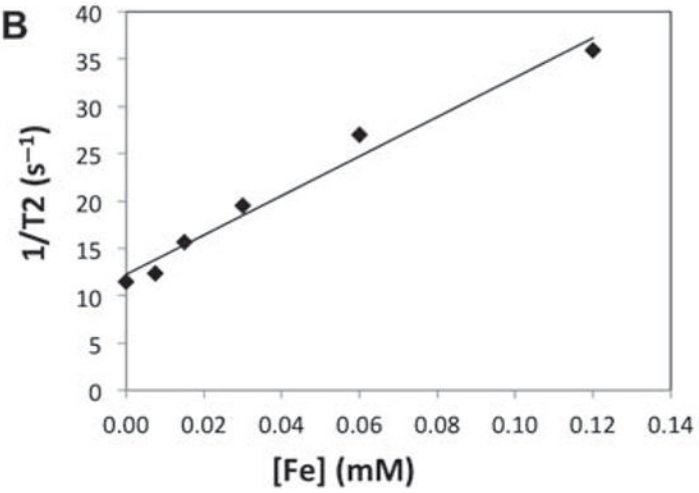

C

Material	Composition	Size (nm)	R_2 at 1.5 T ($mM^{-1}s^{-1}$)	R_2 at 4.7 T ($mM^{-1}s^{-1}$)	Magnet (T), condition
SPIO@AuNS	Fe_2O_3 + silica + Au	~90	208	369	room temperature
Feridex	Fe_2O_3 + dextran	~5	171	240	room temperature

Figure 2.

(A) T_2-weighted MRI images of SPIO@AuNS in water at 0.00446 to 0.223 mM Fe_2O_3 (vial 1 had the lowest concentration, and vial 5 had the highest). (B) SPIO@AuNS relaxivities at different iron concentrations, obtained with a 1.5 T MRI scanner (at room temperature). (C) Relaxivities of SPIO@AuNS and Feridex obtained with 1.5 T and 4.7 T MRI scanners.

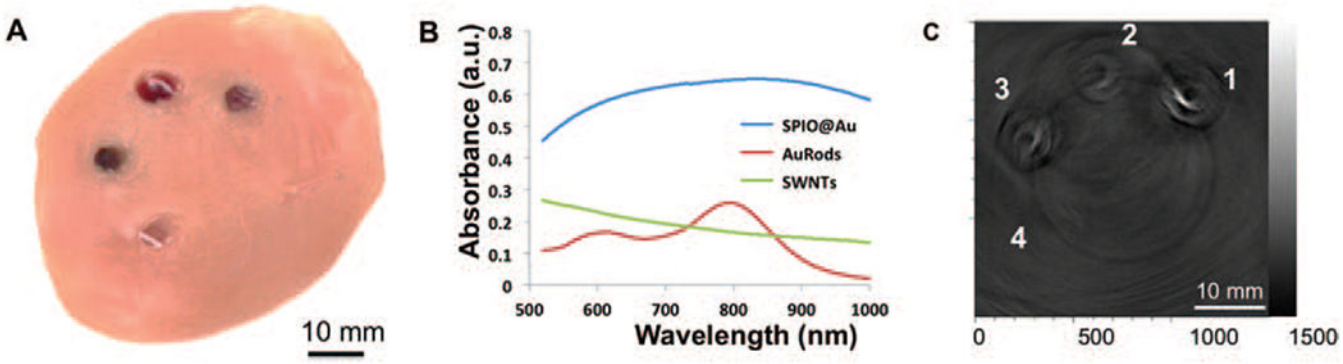

Figure 3.

Photoacoustic (PA) imaging of deeply embedded objects. (A) Agarose gels containing SPIO@AuNS (1), AuRods (2), or SWNTs (3) without any contrast agent and a control gel (4) were embedded in a 1-cm-thick piece of chicken breast muscle, which was then placed under another, 1-cm-thick piece of chicken breast muscle. (B) UV-vis absorption spectra of the different nanomaterials. (C) Corresponding two-dimensional PA image at a depth of 1.0 cm from the laser-illuminated surface.

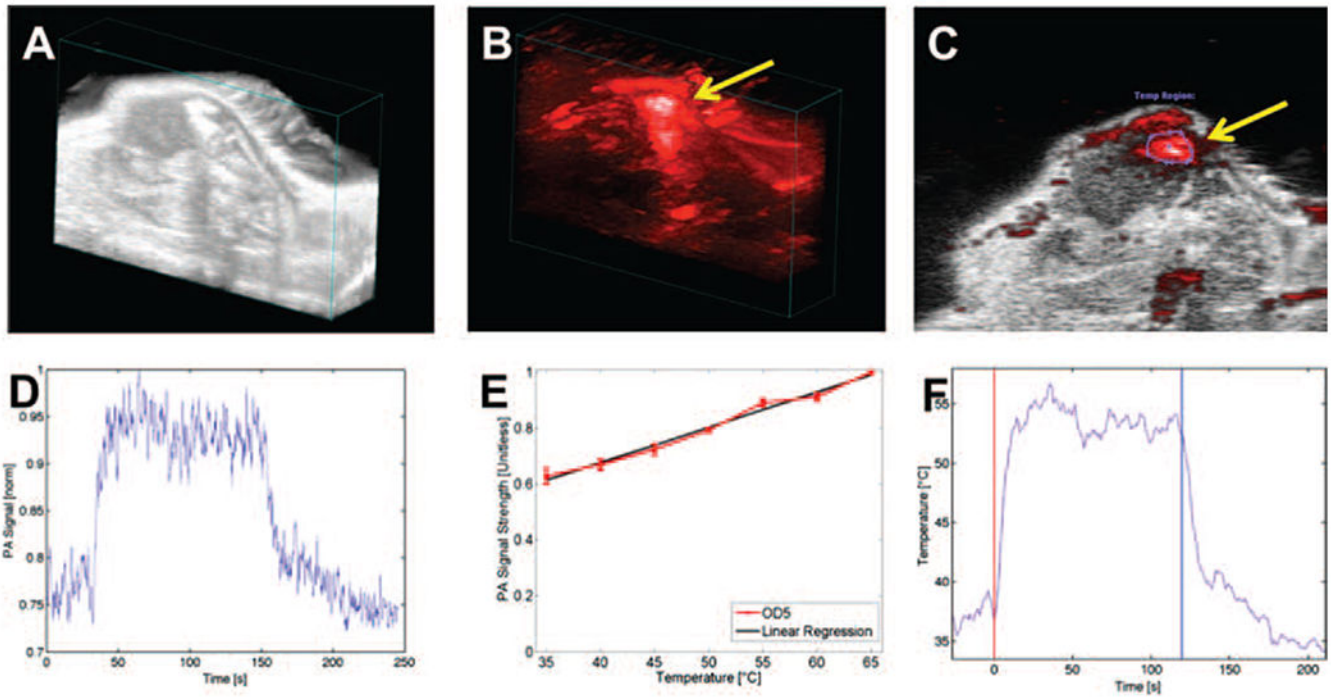

Figure 4.

In vivo photoacoustic (PA) imaging of mouse tumors following intratumoral injection of SPIO@AuNS and irradiation with an NIR laser. (A) Ultrasonogram of a tumor xenograft obtained in B mode (B) PA image of a tumor injected with SPIO@AuNS (C) overlaid PA and B-mode ultrasound images. (D) PA signal amplitude over time. A baseline PA signal was recorded for 40 s, and then laser treatment was delivered for 3 min. (E) The PA signal increased linearly with temperature, as determined with a phantom in a heated water bath. OD5: optical density 5. (F) Conversion of PA signal to temperature using the equation derived from the line in panel E. The red vertical line indicates the start of laser treatment, and the blue vertical line indicates the end of laser treatment.

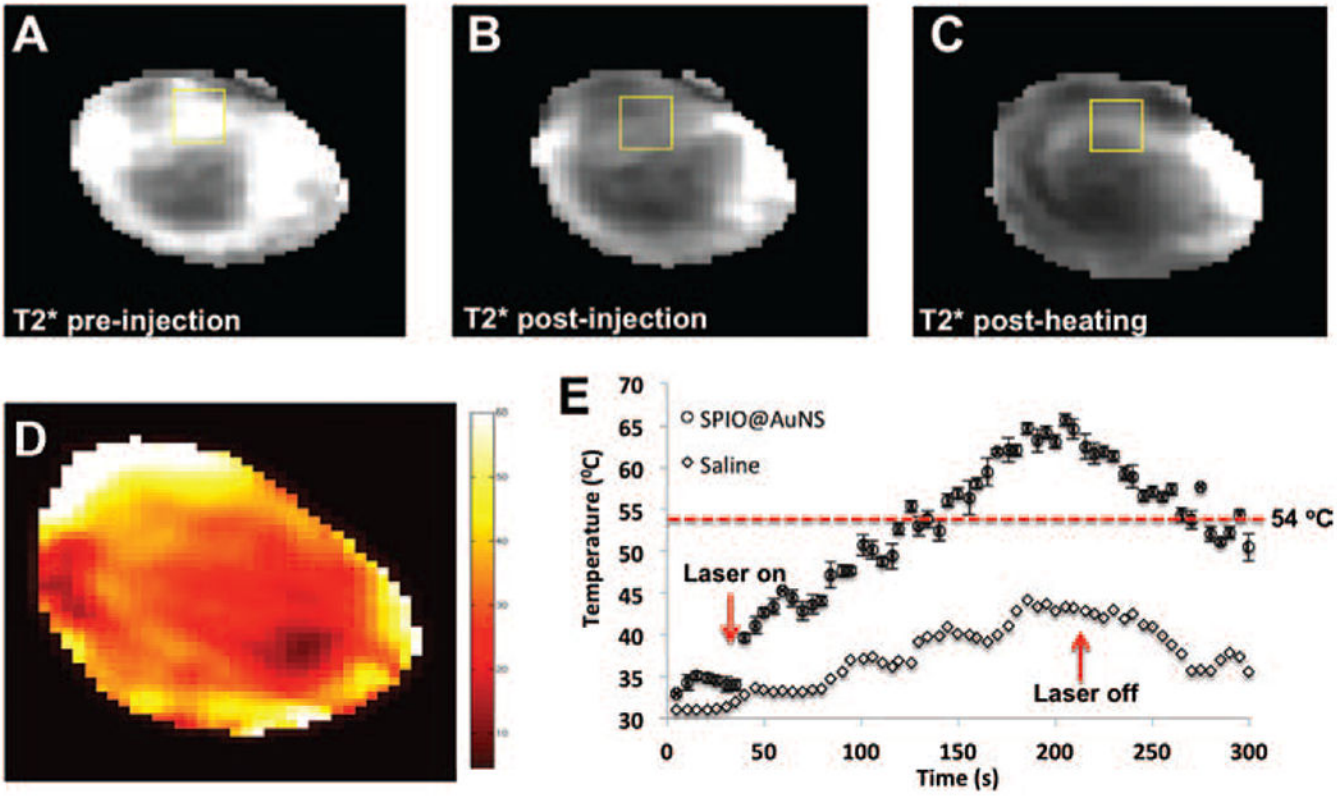

Figure 5.

Representative T_2^*-weighted MR images of mouse 4T1 tumors before (A) and after (B) injection of SPIO@AuNS and after NIR laser irradiation (C). The darkening of the tumor after the injection of SPIO@AuNS indicates a decrease in T_2^*. (D) *In vivo* MRTI map of a tumor injected with SPIO@AuNS immediately after laser treatment. Twenty-four hours after injection, 4T1 tumors were irradiated with an 808-nm laser (180 s, 4 W/cm^2). (E) Temperature elevation over time in tumors injected with SPIO@AuNS or with saline as a control (no nanoparticles). Only in tumors injected with SPIO@AuNS did the temperature rise above the 54 °C threshold (dotted line) for ensuring irreversible thermal ablation of tumors cells. The treatment volume from which the temperature values were obtained is boxed in panel D.

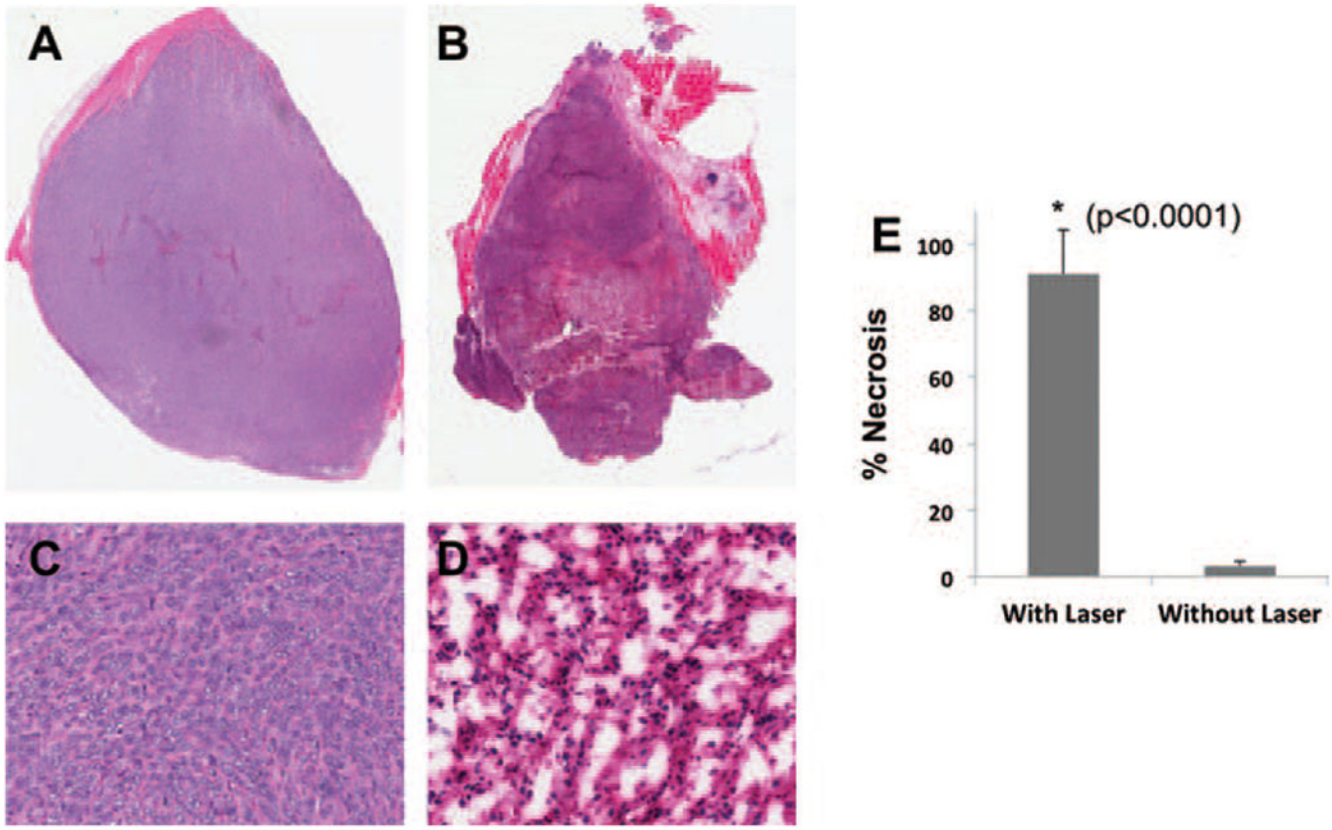

Figure 6.

Representative hematoxylin-eosin-stained sections of 4T1 tumors injected with SPIO@AuNS, with (B, D) or without (A, C) NIR surface laser treatment (4 W/cm^2 for 3 min). The percentage of tumor necrosis in laser-treated mice was significantly higher than that in mice that did not receive laser treatment (91% vs. 3.2%, p <0.0001).

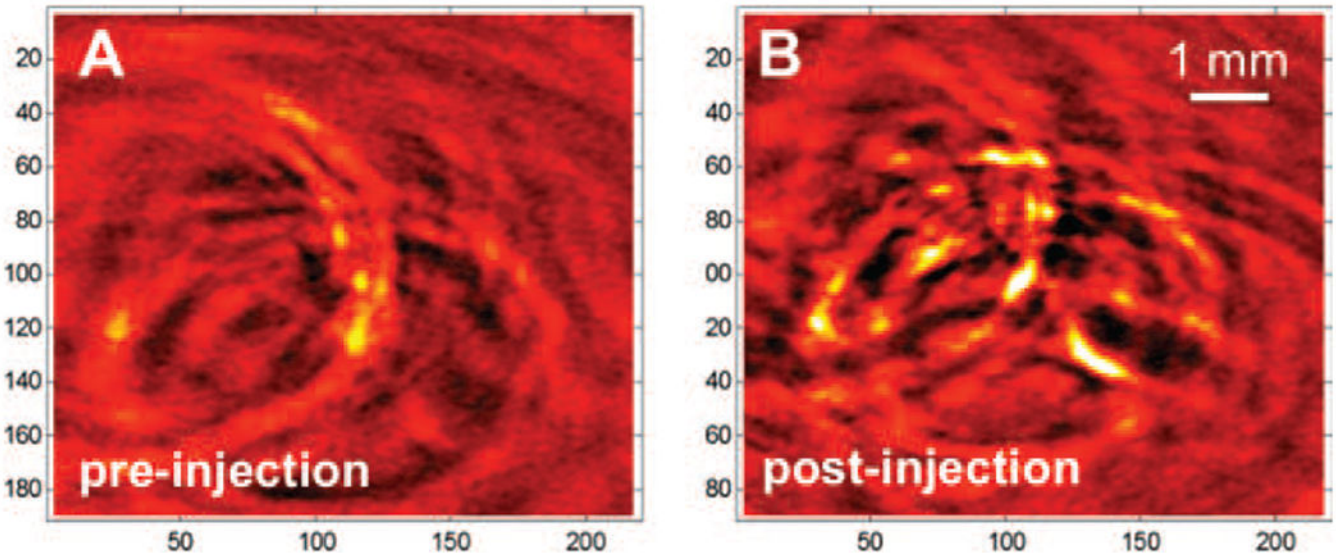

Figure 7.

Representative *in vivo* PA images of a mouse tumor, acquired with an NIR laser at a wavelength of 808 nm before SPIO@AuNS injection and 2 h after intravenous injection of 200 μL of a SPIO@AuNS solution (100 μg/mL).